Mon. Not. R. Astron. Soc. **000**, 000–000 (0000) Printed 26 May 2020 (MN LATEX style file v2.2)

Application of a helicity proxy to edge-on galaxies

Axel Brandenburg[1,2,3,4⋆] and Ray S. Furuya[5]
[1] *Nordita, KTH Royal Institute of Technology and Stockholm University, Roslagstullsbacken 23, SE-10691 Stockholm, Sweden*
[2] *Department of Astronomy, AlbaNova University Center, Stockholm University, SE-10691 Stockholm, Sweden*
[3] *JILA and Laboratory for Atmospheric and Space Physics, University of Colorado, Boulder, CO 80303, USA*
[4] *McWilliams Center for Cosmology & Department of Physics, Carnegie Mellon University, Pittsburgh, PA 15213, USA*
[5] *Institute of Liberal Arts and Sciences, Tokushima University, Minami Jousanajima-machi 1-1, Tokushima 770-8502, Japan*

26 May 2020, Revision: 1.132

ABSTRACT
We study the prospects of detecting magnetic helicity in galaxies by observing the dust polarization of the edge-on galaxy NGC 891. Our numerical results of mean-field dynamo calculations show that there should be a large-scale component of the rotationally invariant parity-odd B polarization that we predict to be negative in the first and third quadrants, and positive in the second and fourth quadrants. The large-scale parity-even E polarization is predicted to be negative near the axis and positive further away in the outskirts. These properties are shown to be mostly a consequence of the magnetic field being azimuthal and the polarized intensity being maximum at the center of the galaxy and are not a signature of magnetic helicity.

Key words: dynamo — MHD — polarization — turbulence — galaxies: magnetic fields — galaxies: individual: NGC 891

1 INTRODUCTION

The magnetic fields of spiral galaxies possess a clear large-scale component along with a fluctuating component of comparable strength (Beck et al. 1996; Han 2017). Owing to the presence of turbulence in the interstellar medium (ISM), there is significant turbulent diffusion, which would destroy the large scale magnetic field on a time scale of less than a billion years (Shukurov 1998), unless there is a correspondingly strong anti-diffusive mechanism. The best known mechanism for explaining the origin and maintenance of galactic large-scale magnetic fields is the α effect (Parker 1955; Steenbeck et al. 1966). In the context of galactic dynamo theory, it was first explored by Parker (1971) and Vainshtein & Ruzmaikin (1971). The existence of the α effect requires a violation of statistical mirror symmetry, which implies the presence of magnetic helicity. It is important to assess the validity of the dynamo models toward a more comprehensive understanding of how a galaxy forms its structure and how magnetic fields regulate the cycle of the ISM by enhancing and suppressing star-formation activity in a galaxy. However, there is no explicit evidence that the α effect really does operate in galaxies.

Methods for measuring the helicity of the magnetic field in our Galaxy and in distant galaxies have been proposed on several occasions in recent years (Volegova & Stepanov 2010; Junklewitz & Enßlin 2011; Oppermann et al. 2011; Brandenburg & Stepanov 2014; Horellou & Fletcher 2014). Measuring this for edge-on galaxies may be particularly advantageous, because we can then see both the upper and lower disc planes simultaneously. However, to measure the magnetic helicity, one needs the full magnetic field vector. Unfortunately, the linear polarization parameters Stokes, Q and U, only allow one to determine the magnetic field direction up to a 180° ambiguity. For this reason it is preferable to work directly with the Stokes parameters and to determine from them a helicity proxy. The quantity of interest is then the parity-odd contribution to the rotationally invariant constituent of the linear polarization, or possibly the correlation between the parity-even and parity-odd polarizations (Kamionkowski et al. 1997; Seljak & Zaldarriaga 1997). This is a relatively new and unexplored technique, which has recently been applied to the Sun's magnetic field (Brandenburg et al. 2019, hereafter BBKMRPS); see also Brandenburg (2019) and Prabhu et al. (2020) for subsequent applications to the global solar magnetic field and to solar active regions, respectively. The original motivation came from Kahniashvili et al. (2014) in the cosmological context.

The attributes parity-even and parity-odd mean the same as mirror-symmetric and mirror-antisymmetric—at least in a statistical sense. For example, a cyclone on a weather map is not statistically mirror-symmetric. In fact, a cyclone in the Northern hemisphere looks like a mirror image of a cyclone in the Southern hemisphere. A cyclone is therefore statistically mirror antisymmetric. The underlying physical quantity is the kinematic helicity. It is a pseu-

⋆ E-mail:brandenb@nordita.org

doscalar, because it changes sign when the system is viewed through a mirror or under parity transformation. The pressure, by contrast, is a scalar; it behaves similarly in the North and the South in that it decreases in a cyclone, for example.

In dynamo theory, one distinguishes quadrupolar and dipolar magnetic fields, whose symmetry about the equator is even and odd, respectively. As a continuous measure of this, one defines the ratio of the difference of the energies contained in the symmetric and antisymmetric parts, divided by their sum. This quantity is sometimes also called parity (Brandenburg et al. 1989), but it is not a pseudoscalar and is therefore, in this sense, a misnomer.

Before we define the parity-even and parity-odd constituents of linear polarization, let us emphasize that these quantities are, at best, a proxy of magnetic helicity. As was already demonstrated in BBKMRPS and Bracco et al. (2019a), there cannot be a detailed correspondence with helicity, because polarization is only defined with respect to a plane. If the velocity or magnetic field are statistically isotopic, these fields can still be fully helical (Moffatt 1978), but a planar image of a cyclone could, with equal probability, also be seen from its back side, so it would appear like its mirror image. Of course, turbulence in galaxies is inhomogeneous, i.e., its statistical properties are not the same in different places. An observer can tell whether one is observing from the outside or the inside. Therefore, there is a chance (but no guarantee) that a particular polarization pattern is preferred over its mirror image. Rotating convection, inspected from the top surface, is such an example in the context of solar turbulence. The magnetic field in our Galaxy is another example (Brandenburg & Brüggen 2020, hereafter BB20).

Let us emphasize at this point that the use of the parity-odd constituent of linear polarization as a proxy of magnetic helicity does not explicitly require information about the line-of-sight component of the magnetic field. Faraday rotation measurements are therefore not invoked in our study. As was already discussed in Brandenburg (2019), it is not clear at this point how this could even be done. This can be regarded as a disadvantage, but we have to keep in mind that our technique is not trying to reconstruct the magnetic field. Instead, we use the appropriate and complete description of linear polarization to obtain a pseudoscalar without the need for a questionable reconstruction. It is simply a new diagnostic and it is then up to us to find out whether or not it has anything to do with magnetic helicity. It might also have to do with differential rotation, or with a combination of helicity and differential rotation.

The purpose of the present work is to learn more about the theoretically expected patterns for edge-on galaxies by taking NGC 891 as a representative case. Here, we consider a numerical solution of a simple galactic mean-field dynamo of $\alpha\Omega$ type. The magnetic field is generated by the α effect (Krause & Rädler 1980) and differential rotation. We embed a flat dynamo in a Cartesian domain. We do this by choosing a distribution of α that is concentrated about the midplane and has opposite signs above and below it. The magnetic diffusivity is taken to be constant. The radius of the disc is assumed to be 15 kpc. Some of our models are similar to those of Brandenburg et al. (1993), who discussed the application to two particular edge-on galaxies, NGC 891 and NGC 4631. Recent multi-wavelength continuum emission studies between wavelengths of 3.6 μm and 2.6 mm clearly show that the properties of dust grains in the ISM of NGC 891 are similar to those in the Milky Way (Hughes et al. 2014). This makes this galaxy an ideal laboratory for testing not only our model, but also for studying the roles of magnetic fields in galaxies in general.

At this point, our goal is to identify characteristic and distinguishing features in the polarization pattern rather than to construct a detailed prediction for NGC 891, which would include a detailed treatment of the wind, as was done in Brandenburg et al. (1993), and more recently by Moss & Sokoloff (2017). The wind can both enhance and suppresses dynamo action (Chamandy et al. 2015). Most importantly, however, it can make the polarization orientation more vertical and thus closer to what is observed (Elstner et al. 1995). There is also great interest in modeling the magnetic field in the galactic halo (Sokoloff & Shukurov 1990; Brandenburg et al. 1992), where significant magnetic field strengths are observed (Howk & Savage 1999; Wiegert et al. 2015; Krause 2019; Krause et al. 2020).

2 PARITY-EVEN AND PARITY-ODD POLARIZATIONS

In the context of polarimetry of the cosmic microwave background radiation, one commonly decomposes the linear polarization into the parity-even E and the parity-odd B polarizations. These E and B fields are defined as the real and imaginary parts of a certain quantity R, which is given in terms of a global expansion of linear polarization on the full sphere of the sky. Here, however, we are only interested in local Cartesian patches in the sky. We can then employ standard Fourier transformation of the complex polarization $P=Q+\mathrm{i}U$ to compute the quantity

$$\tilde{R}(k_x,k_z)=(\hat{k}_x-\mathrm{i}\hat{k}_z)^2\int e^{-\mathrm{i}\boldsymbol{k}\cdot\boldsymbol{x}}P(\boldsymbol{x})\,\mathrm{d}^2\boldsymbol{x}, \tag{1}$$

where the tilde indicates Fourier transformation of R over the spatial coordinates in the projected plane in the sky, which are here the x and z coordinates, so (x,z) is the plane of the sky and y is the line of sight coordinate pointing away from the observer. The real and imaginary parts of R give the E and B polarizations, and $\hat{k}_x$ and $\hat{k}_z$ are the x and z components of the planar unit vector $\hat{\boldsymbol{k}}=\boldsymbol{k}/k$, with $\boldsymbol{k}=(k_x,k_z)$ and $k=(k_x^2+k_z^2)^{1/2}$ being the length of $\boldsymbol{k}$. Thus, we have

$$E(\boldsymbol{x})+\mathrm{i}B(\boldsymbol{x})\equiv R=\int e^{\mathrm{i}\boldsymbol{k}\cdot\boldsymbol{x}}\tilde{R}(\boldsymbol{k})\,\mathrm{d}^2\boldsymbol{k}/(2\pi)^2. \tag{2}$$

The occurrence of the factor $(\hat{k}_x-\mathrm{i}\hat{k}_z)^2$ in Eq. (1) is explained by the fact that it is the square of the complex conjugate of the generating function $\hat{k}_x+\mathrm{i}\hat{k}_z$ for pure E and B modes. Multiplying this by a phase factor $e^{\mathrm{i}\pi n/4}$ samples E patterns for $n=0$ and 2 and B patterns for $n=1$ and 3 in a continuous fashion (Brandenburg 2020); see also standard text books in the field (Durrer 2008) and reviews Kamionkowski & Kovetz (2016).

When comparing the signs of E and B with other work in the literature, one should be aware of the possibility of different sign conventions; see Brandenburg (2019) and

Table 1. Signs of E and B reported in the literature for characteristic features in the Northern hemisphere for various cases and viewing directions.

case	E	B	view	reference
rotating convection	−	−	face-on	BBKMRPS
solar active regions	−	+	face-on	Prabhu et al. (2020)
Galaxy	−	−	Sun	BB20
spherical dynamo	−	−	edge-on	Brandenburg (2019)
edge-on galaxies	−	−	edge-on	present work

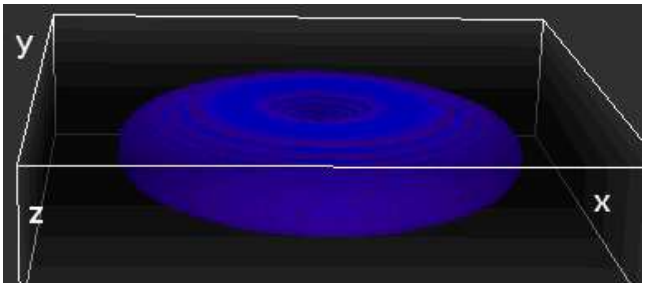

Figure 1. Three-dimensional visualization of $\boldsymbol{B}^2$ for Model II. The nearly edge-on observer sees the xz plane and is located in the negative y direction.

Prabhu et al. (2020) for a more detailed discussion. We refer to Appendix A for a comparison relevant to the present work.

The E polarization corresponds to cross-like magnetic field patterns if $E > 0$ and to ring-like magnetic field patterns if $E < 0$; see Figure 2 of BBKMRPS. Positive (negative) B polarizations, on the other hand, correspond to clockwise (counterclockwise) inward spiraling patterns. The two latter patterns are evidently parity-odd, because that for $B > 0$ becomes the pattern for $B < 0$ under parity transformation. By contrast, the E patterns do not change under parity transformation. In this paper, we consider an edge-on galaxy, so we are not concerned with the grand spiral design of galaxies. This, too, could in principle lead to B polarization (BB20), but this would require the galaxy to be viewed face-on.

Even when the system is inhomogenous and a finite B emerges, it is not yet clear what its sign is. This uncertainty may be mainly due to the fact that the B polarization has not yet been studied under sufficiently many circumstances. It does depend on the spatial magnetic field pattern produced by the system. The experience gathered so far is somewhat sketchy; see Table 1 for a summary. The results depend not only on the nature of the physical system under consideration, but also on the viewing direction. Viewing a disk galaxy from the outside, for example edge-on, will produce the opposite result for the B polarization as viewing from the inside, for example when viewing our Galaxy from the position of the Sun, as was done by BB20.

Looking at Table 1, there seems to be agreement regarding a negative sign for E, but B can have either sign, depending on circumstances. In rotating convection, $E < 0$ and $B < 0$; see Fig. 10 of BBKMRPS. In solar active regions; $E < 0$ but $B > 0$; see Fig. 5 of Prabhu et al. (2020). Also, within $\pm 10^\circ$ near the Galactic midplane, $E < 0$ and $B < 0$ ($B > 0$) for the azimuthally averaged polarization in the Northern (Southern) hemisphere; see BB20. For a spherical mean-field dynamo, Fig. 1 of Brandenburg (2019) shows positive E and B in the North, but this corresponds to $E < 0$ and $B < 0$. This would agree with the present paper if we took E near the axis and B in the first and third quadrants in an edge-on view. We emphasize again that these properties with respect to North and South are independent of the question of whether the magnetic field is even or odd about the equatorial plane. Determining this with Faraday rotation measurements is certainly of interest, but it is not explicitly connected with our helicity proxy.

3 THE MODEL

We adopt the galactic dynamo model of Brandenburg (2015). It is fully three-dimensional, but when computing an edge-on view, we consider a specific xz cross-section through $y = -10\,\mathrm{kpc}$ with the observer being located in the direction $y \to -\infty$; see Fig. 1. Except for one case, where we investigate the magnetic field in the central slice through $y = 0$, we chose the slice $y = -10\,\mathrm{kpc}$ as a compromise that is well in front of the central slice and already sufficiently far into the galaxy to be representative of its field near the periphery. We compute the complex polarization, $P = Q + \mathrm{i}U$, as

$$P = -\epsilon\,(b_x + \mathrm{i}b_z)^2/\boldsymbol{b}_\perp^2, \tag{3}$$

where $\boldsymbol{b}_\perp \equiv (b_x, b_z)$ is the magnetic field vector in the (x, z) plane and ϵ is the emissivity (Alton et al. 2004; Planck Collaboration Int. XIX 2015), which is here assumed to be constant. The observer is at $y \to -\infty$, which is equivalent with the definition of BBKMRPS, where the observer of (b_x, b_y) was at $z \to \infty$, corresponding to the vertical direction in their rotating convection simulations and their view toward the Sun. Next, we compute $R = E + \mathrm{i}B$ using Eq. (2). We then show $E(x, z)$ and $B(x, z)$ at a given position y; see Figs. 2–4. We indicate the polarization angle

$$\chi = \tfrac{1}{2}\mathrm{atan}(\mathrm{Im}P/\mathrm{Re}P), \tag{4}$$

which we also calculate for the pure E and B modes by computing $\tilde{P}_{E/B}(k_x, k_z) = (\hat{k}_x + \mathrm{i}\hat{k}_z)^2 \tilde{R}_{E/B}(k_x, k_z)$ in Fourier space, where $\tilde{R}_E = \tilde{E}$ and $\tilde{R}_B = \mathrm{i}\tilde{B}$.

We adopt a mean-field model where all dependent variables are defined as azimuthal averages indicated by an overbar. The mean magnetic field $\overline{\boldsymbol{B}}$ is expressed in terms of the mean magnetic vector potential $\overline{\boldsymbol{A}}$ as $\overline{\boldsymbol{B}} = \boldsymbol{\nabla} \times \overline{\boldsymbol{A}}$. We solve the $\alpha\Omega$ dynamo equation in its simplest form,

$$\frac{\partial \overline{\boldsymbol{A}}}{\partial t} = \overline{\boldsymbol{U}} \times \overline{\boldsymbol{B}} + \boldsymbol{\alpha} \cdot \overline{\boldsymbol{B}} - \eta_\mathrm{T}\mu_0 \overline{\boldsymbol{J}}, \tag{5}$$

where $\overline{\boldsymbol{U}}$ is the mean flow, $\overline{\boldsymbol{J}} = \boldsymbol{\nabla} \times \overline{\boldsymbol{B}}/\mu_0$ is the mean current density, μ_0 is the vacuum permeability, $\boldsymbol{\alpha} = \mathrm{diag}\,(\alpha_\perp, \alpha_\perp, 0)$ is the α tensor in the limit of rapid rotation (Rüdiger 1978), and η_T is the total (microphysical and turbulent) magnetic diffusivity. The mean flow is composed of toroidal and poloidal components, $\overline{\boldsymbol{U}}_\mathrm{t}$ and $\overline{\boldsymbol{U}}_\mathrm{p}$, respectively, describing the galactic rotation profile and a galactic wind. We use $\overline{\boldsymbol{U}}_\mathrm{p} = W_r\,[1 - \exp(-z^2/2H_W^2)]\,\boldsymbol{r}/R$ from Brandenburg et al. (1993) in one case where we include a galactic wind. The

value of W_r determines its strength and H_W is the height above which the wind commences.

In the following we assume the galactic rotation to be represented by a modified Brandt rotation profile of the form $\overline{\boldsymbol{U}}_{\rm t}=\varpi\Omega(\varpi)$, where $\boldsymbol{\varpi}=(x,y,0)$ with $\varpi=|\boldsymbol{\varpi}|$ being the cylindrical radius, and

$$\Omega=\Omega_0/[1+(\varpi/\varpi_\Omega)^n]^{1/n} \tag{6}$$

is the angular velocity with $\Omega_0=$ const characterizing the rigid rotation law for $\varpi<\varpi_\Omega$, and $\varpi_\Omega=3\,$kpc is the radius where the rotation law attains constant linear velocity $V_0=\Omega_0\varpi_\Omega$. The exponent n allows one to make the transition from rigid to constant rotation sharper, but in the models presented below we used the rather moderate value $n=2$ for Model I and $n=3/2$ for Models II–IV (see below).

For the α effect we assume a nonlinear (α-quenched) formulation (Ivanova & Ruzmaikin 2008) for the horizontal components of the α tensor and choose

$$\alpha_\perp=\frac{\alpha_0}{1+Q_\alpha\overline{\boldsymbol{B}}^2/B_{\rm eq}^2}\frac{z}{H_\alpha}\exp\left(-\frac{z^2}{H_\alpha^2}\right)f_\alpha(\varpi)\,g_\alpha(\varpi), \tag{7}$$

where H_α is the disc height for the α effect, α_0 quantifies its strength, and $f_\alpha(\varpi)$ and $g_\alpha(\varpi)$ are radial profiles that we apply in Models II–IV. In those cases, we use

$$f_\alpha(\varpi)=[1-{\rm erf}(\varpi/\varpi_\alpha)]/2 \tag{8}$$

to introduce a radial cutoff at $\varpi=\varpi_\alpha=15\,$kpc, and

$$g_\alpha(\varpi)=[1+(\varpi/\varpi_{\alpha\Omega})^n]^{-1/n} \tag{9}$$

to allow for an additional radial modulation with $\varpi_{\alpha\Omega}=\varpi_\Omega$ in Models II–IV, such that $\alpha_\perp$ is proportional to the local angular velocity, as was assumed in the model of Brandenburg et al. (1993), who assumed $\alpha_0=\Omega_0\ell$, with $\ell=0.3\,$kpc being the correlation length. In Model I, on the other hand, $\alpha_\perp$ is independent of ϖ and therefore we put $\varpi_{\alpha\Omega}=\infty$. Note that in both cases, owing to the z/H_α factor in front of the exponential function, $\alpha_\perp$ changes sign about the midplane. This reflects the opposite orientation of the Coriolis force on the two sides of the midplane. For comparison, we also present a more complicated case with $W_r=10\,{\rm km\,s^{-1}}$ using $H_\alpha=H_W=0.5\,$kpc (Model III).

We define the equipartition field strength based on the root-mean-square value of the turbulent velocity, $u_{\rm rms}$, as $B_{\rm eq}=\sqrt{\mu_0\rho}\,u_{\rm rms}$; see also Eq. (1) of Beck et al. (2019). Using $u_{\rm rms}=10\,{\rm km\,s^{-1}}$ and $\rho=2\times10^{-24}\,{\rm g\,cm^{-3}}$, we have $B_{\rm eq}=5\,\mu$G (Brandenburg et al. 1993), which is the value we use in all of our models. For orientation we note that the line-of-sight and plane-of-sky components of the magnetic field toward galactic molecular clouds are on the order of 1–100 μG, estimated from Zeeman effect measurements (e.g., Crutcher 2012) and dust polarization studies (e.g., Pattle & Fissel 2019), respectively. The mean magnetic field is typically below $10\,\mu$G (Beck et al. 2019). The parameter Q_α is a nondimensional constant that determines the strength of α-quenching, and thereby the overall magnetic field strength. We choose $Q_\alpha=25$, so the resulting mean magnetic field strength attains plausible values of somewhat below $10\,\mu$G.

On the periphery of the computational domain, we assume normal-field conditions, i.e., $\hat{\boldsymbol{n}}\cdot\overline{\boldsymbol{A}}=(\hat{\boldsymbol{n}}\cdot\boldsymbol{\nabla})\times\overline{\boldsymbol{A}}=0$, where $\hat{\boldsymbol{n}}$ is the unit vector normal to the boundary. The initial condition for $\overline{\boldsymbol{A}}(\boldsymbol{x},0)$ is Gaussian distributed white noise of low amplitude. In this paper, we measure lengths in kpc and speeds in $\,{\rm km\,s^{-1}}$, so time is measured in units of 0.98 Gyr. For simplicity, we drop the factor 0.98 when specifying times or inverse times.

Table 2. Parameters of the dynamo models discussed.

	Ω_0 [Gyr^{-1}]	W_r [km s^{-1}]	α_0 [km s^{-1}]	H_α [kpc]	ϖ_α [kpc]	$\varpi_{\alpha\Omega}$	$B_{\rm max}$ [μG]
I	100	0	16	0.2	—	∞	8.7
II	75	0	22	1.5	15	ϖ_Ω	15.6
III	75	10	22	0.5	15	ϖ_Ω	0.72
IV	75	0	-15	1.5	15	ϖ_Ω	0.82

We consider several models. First, we take the one of Brandenburg (2015), which was designed to reflect typical spiral galaxies (Model I). Second, we modify the parameters (rotation curve and α effect) such that they match those of the model of Brandenburg et al. (1993) of NGC 891 (Model II). In both cases, we use $64^2\times16$ mesh points, which proved sufficient to resolve the spatial structure of the magnetic field. Calculations with $128^2\times32$ mesh points produced virtually identical polarization maps. Next, we use a model with a radial wind and a thinner disk, where the polarization pattern resembles more closely the observed ones (Model III). Finally, to study the properties of our diagnostic as a proxy for magnetic helicity in terms of the B polarization, we also present a model with a negative α_0, where we expect the sign of the magnetic helicity to be reversed relative to what it is otherwise (Model IV). However, the nature of the $\alpha\Omega$ dynamo also changes and the most easily excited field is then an oscillatory one, so no direct comparison is possible.

The computations are performed with the Pencil Code (Brandenburg & Dobler 2010) using either Cartesian coordinates (Models I, II, and IV) or cylindrical coordinates (Model III). We emphasize in this connection that we are dealing here with a mean field model, so no sharp structures are expected to occur in such a case. In Table 2 we summarize the various parameters used here. We also give the maximum field strength $B_{\rm max}$.

4 RESULTS

4.1 E and B polarizations

Our models lead to an early exponential growth of the magnetic field and reach saturation after about 10 Gyr. Here we consider only the saturated phase of the models. As a first step, we show in Fig. 2 the E and B polarizations together with the polarized intensity and polarization orientations for Model I from the xz plane near $y=-10\,$kpc. In Fig. 3 we again show the E and B polarizations, but now for Model II. The polarized intensity and polarization orientations show just a horizontal pattern. It is therefore amazing that the decomposition into its rotationally invariant constituents appears so much richer. The primary reason for this is connected just with the spatial variation of the polarized intensity. This is demonstrated in Appendix A, where we show the E and B polarizations for a polarization sig-

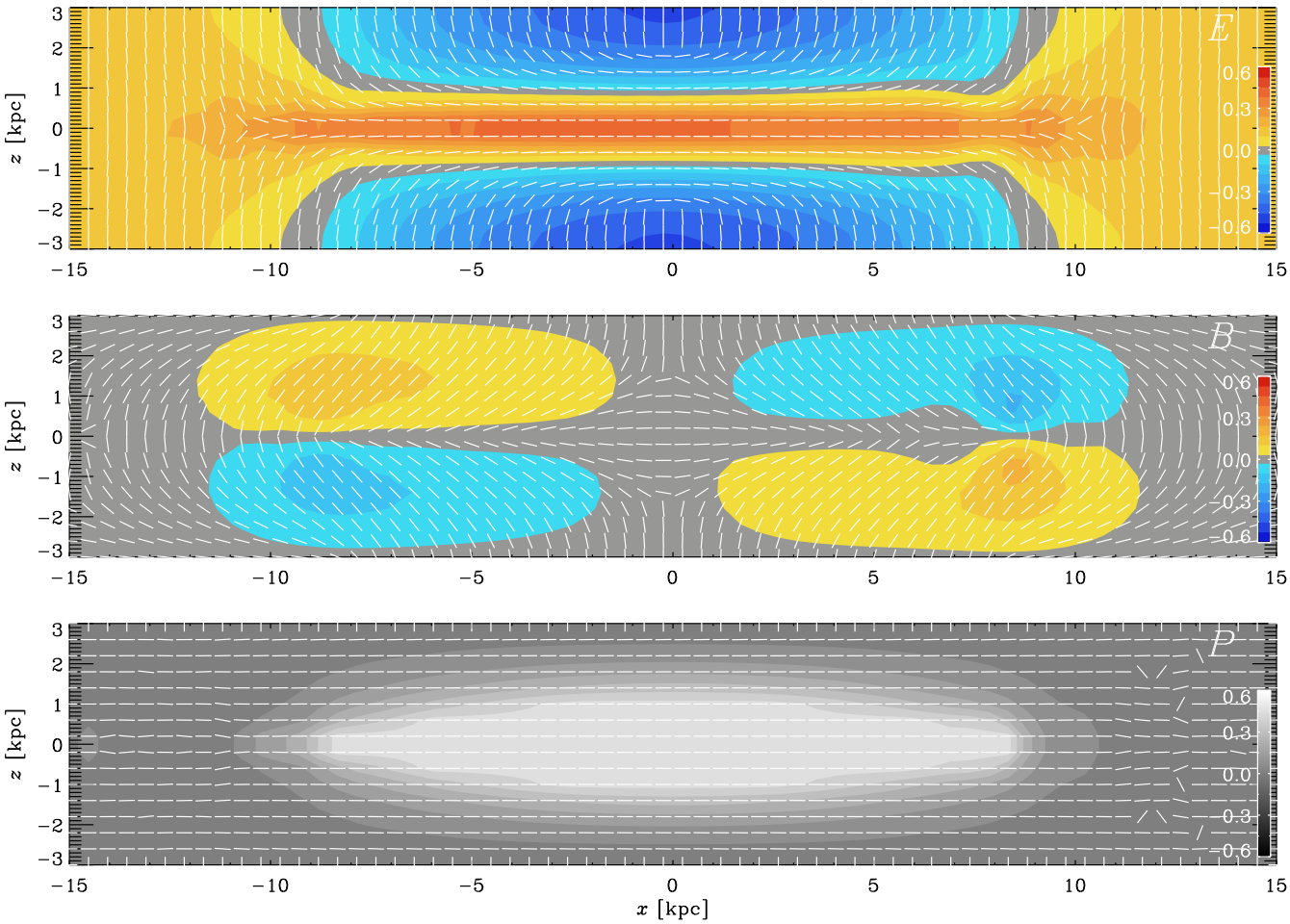

Figure 2. E and B polarizations as well as polarized intensity $|P|$ in an edge-on view of Model I, which is the galactic dynamo model of Brandenburg (2015). The short lines show the corresponding angles. The color scale shows the values of E, B, and $|P|$ in units where $\epsilon = 1$ in Eq. (3); see BBKMRPS.

nal where Stokes $U = 0$ and Stokes Q consists of just a Gaussian.

There are remarkable similarities between the polarization patterns obtained from a Gaussian and those obtained from our dynamo model. This suggests that the information content in the overall pattern seen in Figs. 2 and 3 is not very profound, although more physically meaningful information may still be hidden within the more subtle departures from this overall pattern.

The pixel resolution in Fig. 3 is about 650 pc, which is the spatial resolution when NGC 891 is observed at a distance of 9.6 Mpc (Strickland et al. 2004) with the 14 arcsecond beam of the JCMT at 850 μm wavelength. We see that, in both cases, E is symmetric about the midplane $z = 0$, and B is antisymmetric. Moreover, E is negative in the halo near the axis ($x = 0$) and positive near the midplane further away from the axis. In Model I, however, E is positive at the center ($x = z = 0$), while in Model II it is negative. As expected, B changes sign about the equator. It also changes sign between the two sides of the rotation axis. In the first and third quadrants, the sign is negative, while in the second and fourth, it is positive. The arrow-less vectors associated with the B polarization show a clockwise inward swirl in the first and third quadrants and an anti-clockwise inward swirl in the second and fourth quadrants. This signature seems to be surprisingly independent of the differences between Models I and II. The patterns of E and B are also rather smooth; the typical scale would be the scale height of the magnetic field, which is about 2 kpc. In this context, we must recall that our model can only deliver the mean magnetic field, and that the actual magnetic field must also contain a fluctuating component of smaller scales below 100 pc.

To get a sense of the range of E and B polarization patterns, we show in Fig. 4 the results for a model with a radial wind of just $10\,\mathrm{km\,s^{-1}}$ and a thinner disk; see Model III in Table 2. Here we inspect the plane $y = 0$, where the polarization orientations best resembles those observed in synchrotron emission (Howk & Savage 1999; Wiegert et al. 2015; Krause 2019; Krause et al. 2020). The maximum field strength is here much weaker. This can be explained by the wind advecting the magnetic field away from the disk. In our models, this suppression of the magnetic field might be more effective because of the anisotropic α effect. Interestingly, the E polarization is now strongly negative along the midplane. This is similar to what is seen for our Galaxy viewed from the position of the Sun (BB20). Furthermore,

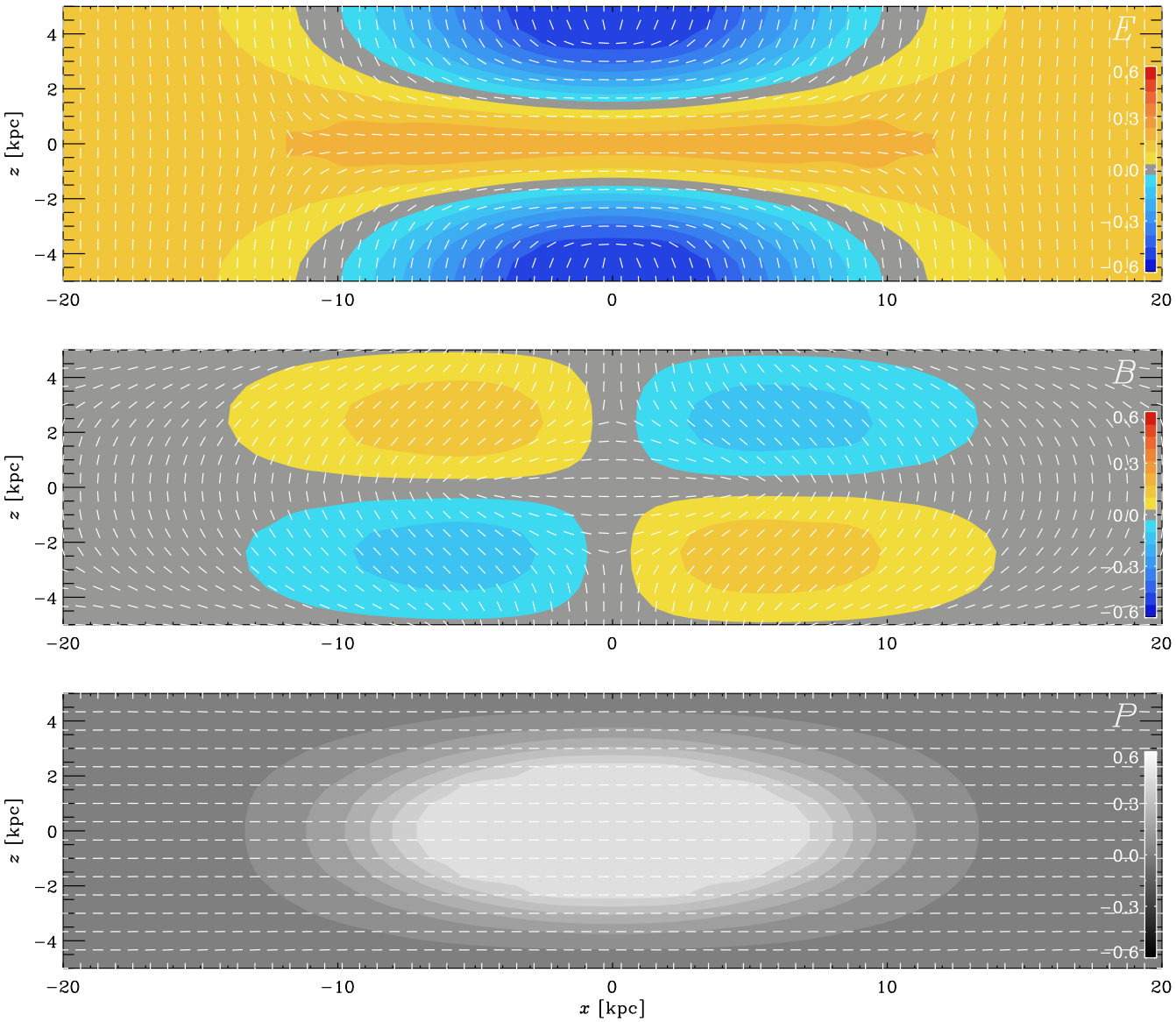

Figure 3. Same as Fig. 2, but for Model II with parameters relevant to NGC 891. Note the pixel resolution of about 650 pc, which corresponds to the 14 arcsecond beam of the JCMT at 850 μm wavelength.

the polarization is now more complicated. The patches with negative (positive) values in the first and third (second and fourth) quadrants are now closer to the axis, and there is an additional such pattern with opposite signs further out.

4.2 Magnetic field and helicity

It is important to realize that neither the helicity of the magnetic field nor any proxy of it can straightforwardly be extracted from just a simple inspection of the morphology of the magnetic field. This is mostly because of the strong dominance of the azimuthal magnetic field over the vertical (z) field in galactic latitude. This becomes clear once again from Fig. 5, where we show vectors of $\boldsymbol{b}_\perp$ superimposed on a color scale representation of b_y. Here, b_z has been scaled by a factor of 20 relative to b_x, but the vertical field still seems almost completely negligible.

It is long known that the magnetic field in galaxies tends to have even symmetry about the equatorial plane (Beck et al. 1996, 2019). This is also the case for all of our models. This means that the azimuthal magnetic field is symmetric about the midplane and the vertical magnetic field is antisymmetric about in the midplane, just as seen from Fig. 5. Note, also, that the strongest magnetic field is found at a distance of about 7 kpc from the center. The results for Model I are similar, except that here the strongest magnetic field occurs at a distance of about 5 kpc from the center.

To make contact with the helicity of the magnetic field in our model, we plot in Fig. 6 a vertical slice of the current helicity density $\overline{\boldsymbol{J}}\cdot\overline{\boldsymbol{B}}$. We can see that $\overline{\boldsymbol{J}}\cdot\overline{\boldsymbol{B}}$ is mostly positive (negative) in the upper (lower) disc plane. This agrees with

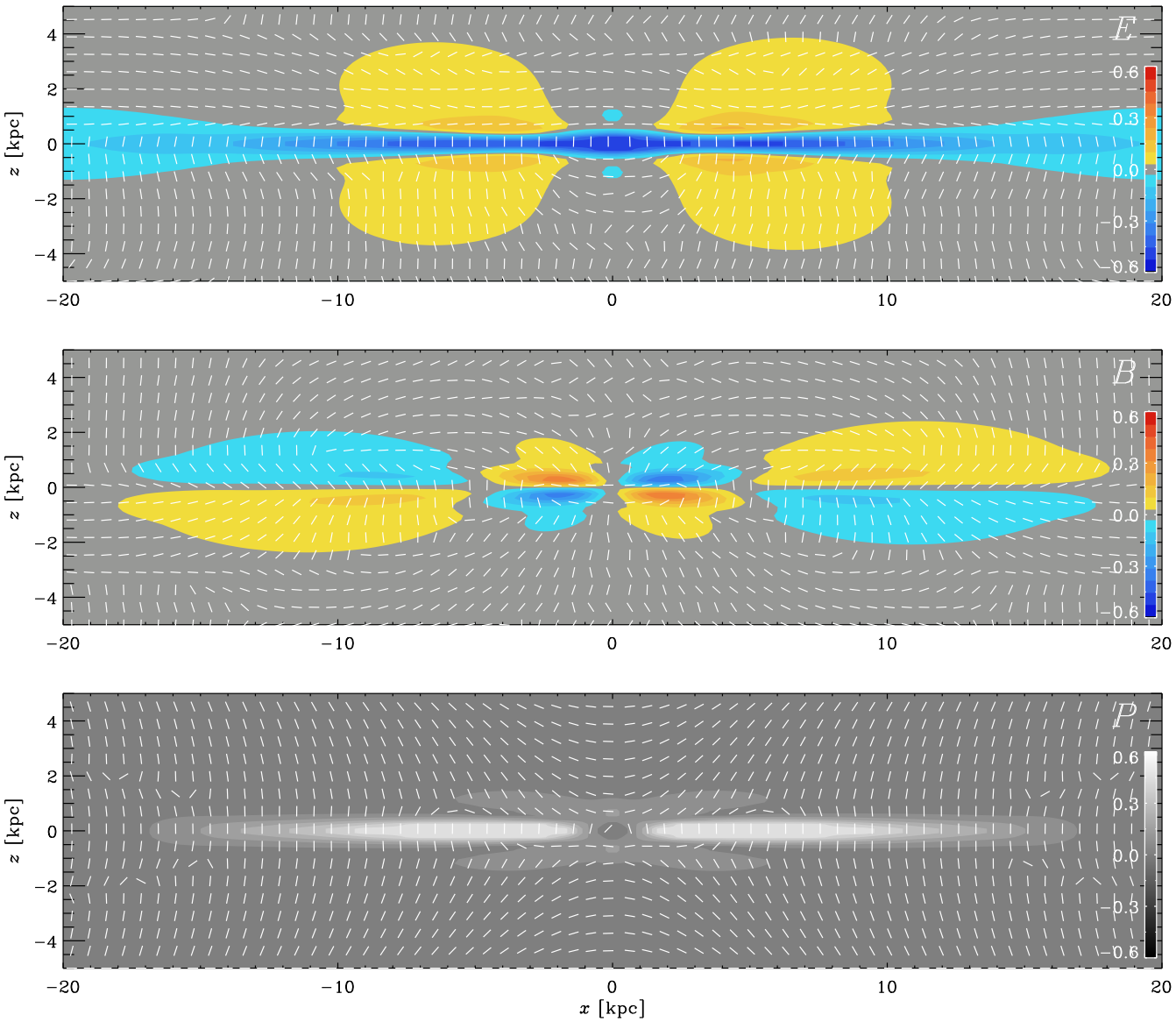

Figure 4. Same as Fig. 2, but for Model III with $W_r = 10\,\mathrm{km\,s^{-1}}$ and $H_\alpha = H_W = 0.5\,\mathrm{kpc}$.

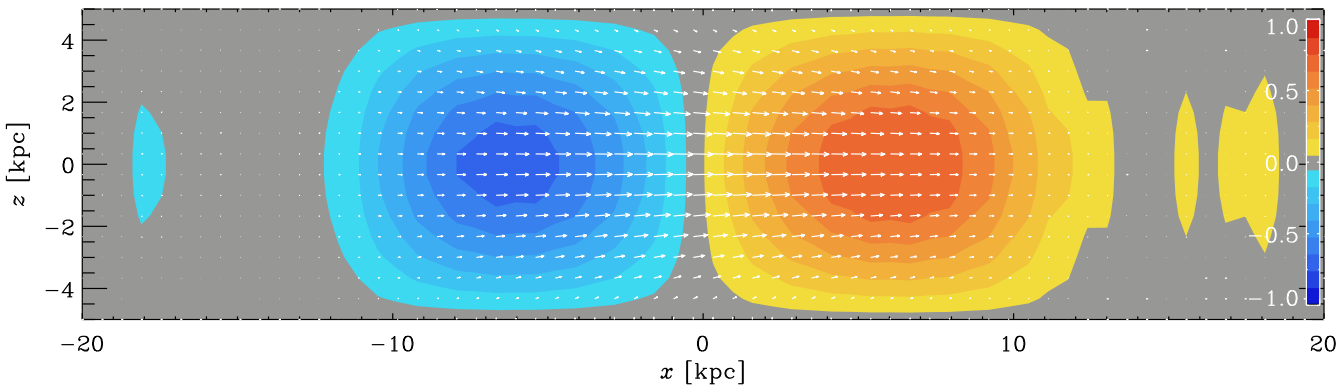

Figure 5. Visualization of the magnetic field for Model II in the same slice for which E and B are shown in Fig. 3. Here, b_z has been scaled by a factor of 20 relative to b_x, but the vertical field still seems almost completely negligible.

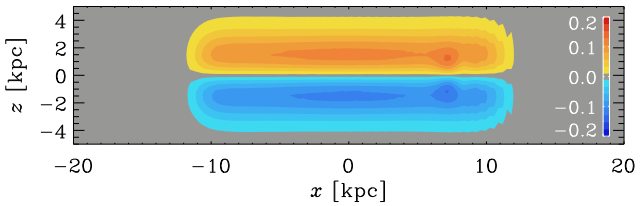

Figure 6. Visualization of the normalized current helicity density, $\mu_0 \overline{\boldsymbol{J}} \cdot \overline{\boldsymbol{B}}$, for Model II at $y = -10\,\mathrm{kpc}$.

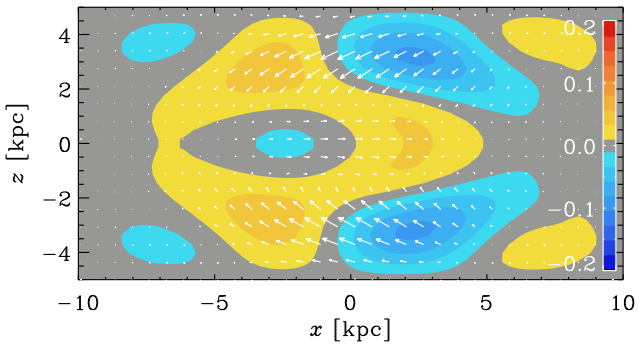

Figure 7. Visualization of the magnetic field, similar to Fig. 5. but for Model IV, at $y = -10\,\mathrm{kpc}$, and b_z has been scaled by a factor of 5 relative to b_x. The plot range in the x direction has been clipped to $\pm 10\,\mathrm{kpc}$.

the sign of $\alpha_\perp$, which is also positive (negative) in the upper (lower) disc plane. For $Q_\alpha = 25$, the normalized current helicity density, $\mu_0 \overline{\boldsymbol{J}} \cdot \overline{\boldsymbol{B}}$, would be in units of $\mu\mathrm{G}^2\,\mathrm{kpc}^{-1}$.

4.3 Negative α and reversed helicity

To give a sense of the range of possibilities for the E and B patterns in models of edge-on galaxies, we now consider Model IV with a negative α_0. As mentioned in Sect. 3, such a model is not simply a mirror image of a model with a positive value of α_0, because the nature of the dynamo also changes. In the present case, the field becomes oscillatory, but retains its even symmetry with respect to the midplane; see Fig. 7 for a visualization of the magnetic field in a cross-section through $y = -10\,\mathrm{kpc}$. Note that the magnetic field

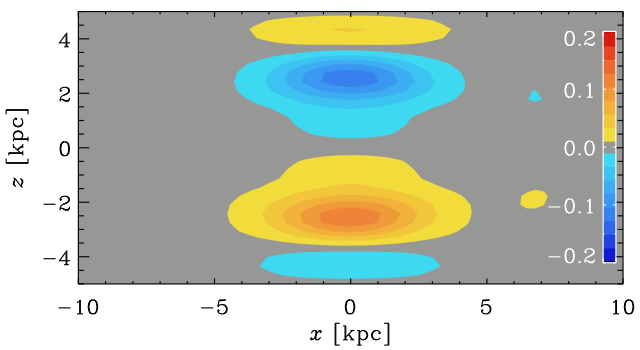

Figure 8. $\mu_0 \overline{\boldsymbol{J}} \cdot \overline{\boldsymbol{B}}$, similar to Fig. 6, but for Model IV, and again at $y = -10\,\mathrm{kpc}$.

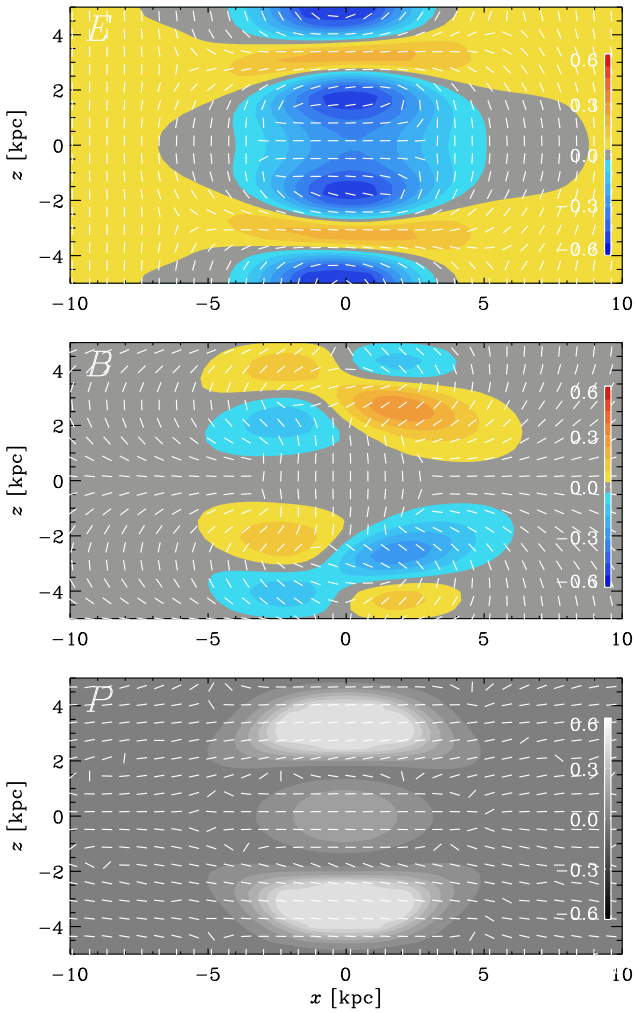

Figure 9. Same as Fig. 2, but for Model IV with negative α_0 at an arbitrarily chosen time. The plot range in the x direction has been clipped to $\pm 10\,\mathrm{kpc}$.

is fairly much confined within a cylindrical radius of 10 kpc. This is why we have clipped in Fig. 7 (and the following two figures) the x range beyond $\pm 10\,\mathrm{kpc}$. However, the numerical calculations have been carried out, just as before, in the larger domain with $|x|, |y| \leq 20\,\mathrm{kpc}$.

To verify that the magnetic helicity has indeed changed sign, we show in Fig. 8 the current helicity, again through the plane $y = -10\,\mathrm{kpc}$. We see that $\overline{\boldsymbol{J}} \cdot \overline{\boldsymbol{B}}$ is now indeed negative in the upper disc plane, but there is an additional sign change close to the edge of the domain.

Finally, the resulting E and B polarizations at $y = -10\,\mathrm{kpc}$ are shown in Fig. 9. Note that B has changed sign with respect to Figs. 2 and 3, at least sufficiently close to the midplane. Closer to the boundaries at $z = \pm 5\,\mathrm{kpc}$, this sign has changed again, somewhat similarly to what was seen in Fig. 8 for $\overline{\boldsymbol{J}} \cdot \overline{\boldsymbol{B}}$. The E polarization is somewhat different than before, although the basic features are unchanged: it is negative near the axis and positive further away from it, except right at the midplane. Within the midplane, the negative sign of E near the axis extends now also to larger radii.

Unlike Fig. 3, the polarized intensity now shows con-

centrations a certain distance away from the midplane. The polarization orientations are still mostly horizontal, so the basic phenomenology explained in Appendix A still applies. This explains then why the E and B polarizations in Fig. 8 show a doubling of the features seen in Fig. 3.

5 DISCUSSION AND FUTURE PROSPECTS

Edge-on galaxies provide an opportunity to study some basic aspects of magnetic fields in galaxies. This can have implications for the dynamo interpretation of their generation. Our preliminary investigation based on simple models suggests that the E polarization is positive near the disc midplane and away from the axis, where it tends to outline star-like patterns in the magnetic field, while in the halo near the axis it is negative, corresponding to ring-like patterns in the magnetic field; see the top panel of Fig. 2. The B polarization is negative in the first and third quadrants and outlines counterclockwise inward spiraling patterns, while in the second and fourth quadrants, we have positive values, corresponding to clockwise inward spiraling patterns; see the bottom panel of Fig. 2. Again, we emphasize here that our discussion of spiraling polarization patterns concerns the edge-on view of the B polarization and is not connected with the spiraling appearance of galaxies viewed face-on.

Our hope is that the predictions for the signs of the E and B polarizations could soon be verified observationally. In addition to utilizing already existing synchrotron polarimetry data, we discuss here the possibility of using observations of dust polarization. Dust polarization observations have proven to be an excellent tool to measure the orientation of the magnetic field in star-forming regions and to assess the relative magnitudes of the mean and turbulent components of the field (Hildebrand et al. 2009). Linear polarization imaging provide the orientation of the plane-of-sky magnetic field lines, as non-spherical dust grains tend to align with their short axis perpendicular to the direction of the magnetic field, giving rise to linear polarization of the emission. As discussed by Andersson et al. (2015), the radiative alignment torque (RAT) theory is the most widely accepted mechanism for interstellar dust grains to align in a realistic environment; see also Bracco et al. (2019b). All-sky dust polarization imaging by *Planck* at 850 μm have already revealed well-defined magnetic field patterns in the ISM from Galactic scales down to molecular cloud scales of $\gtrsim 10$ pc. Because there are no observational studies to test such a mechanism toward a galaxy with a spatial resolution of 10^2–10^3 pc, it is important to assess the validity of such a mechanism.

Although a size of $\gtrsim 10$ pc is still one or two orders of magnitude larger than that of dense cloud cores where stars and stellar cluster form, it is worth attempting to investigate the magnetic-field structure to study the physical conditions of $\lesssim 10$ pc-scale molecular cloud formation. Submillimeter (submm) emission polarimetry is sensitive to tracing the column density of the cold ($T \lesssim$ a few times 10 K) ISM, whereas near-infrared (NIR) absorption polarimetry may have suffered from scattering, while cm-wavelength radio polarimetry may already begin to be affected by Faraday rotation. Indeed, recent polarization observations with SOFIA HAWC+ toward the archetypical starburst galaxy M 82 at 53 and 154 μm (Jones et al. 2019) have clearly demonstrated that submm/FIR emission polarimetry offers another way of probing the magnetic field structure by observing entrained dust grains by the super galactic wind. The authors did not identify any component expected from the large-scale dynamo field. Nevertheless, as the next step, it is worth considering longer wavelength polarimetry at 850 μm toward the edge of a galaxy to unveil the magnetic-field structure in the cold ISM of that galaxy. This would give us a more specific hint at how the magnetic field in a galaxy is maintained against diffusion by turbulence. Moreover, we point out that previous Herschel PACS and SPIRE imaging at 100, 160, and 250 μm revealed that NGC 891 is rich in dust grains—even toward its halo; the scale height of the dusty halo is 1.44 ± 0.12 kpc (Bocchio et al. 2016). These authors showed that $\sim$ 2–3% of the mass of the dust is present further than 2 kpc from the midplane. This agrees with the analysis from the 450 and 850 μm emission taken with SCUBA (Alton et al. 1998). We therefore argue that the method proposed in this work may be feasible; it is complementary to the conventional two methods (radio synchrotron and NIR polarimetry).

At wavelengths of 850 μm, the emission is optically thin as shown by the graybody-fitting at the submm/FIR spectral energy distribution (SED); see Fig. 3 in Alton et al. (1998). Their SED analysis clearly favors a frequency index of grain emissivity, β, of 2 rather than 1.5, suggesting that grains' properties are ISM-like, i.e., not evolved like those seen in protoplanetary disks. These results were later confirmed by multi-wavelength imaging studies adding Spitzer, WISE, and Herschel data (Whaley et al. 2009; Hughes et al. 2014). The grain emissivity, its frequency index, and the dust temperature are similar to those measured in $\gtrsim 10$ pc-scale galactic molecular clouds where submm polarization imaging were performed (Matthews et al. 2009; Ward-Thompson et al. 2017). However, caution must be exercised because polarization properties of grains on galaxy scales are poorly known. Nevertheless, given the highly-enhanced sensitivity of the current instrument, SCUBA-2 plus the POL-2 polarimeter system of $\sim 4\,\mathrm{mJy\,beam^{-1}}$ in polarization intensity for a typical observation, we do believe that 850 μm polarimetric observations toward NGC 891 could help to assess signs of handedness. As of today, no polarization data in FIR or submm are yet available for NGC 891. However, intensity maps of NGC 891 at 850 μm show two "blobs" or "knots" at a distance of about 4–5 kpc from the center (Haas et al. 2002; Whaley et al. 2009). This could also be suggestive of a ring-like magnetic field, similarly to what is seen in Fig. 5. This would be analogous to the ring-like magnetic field of M 31 (Beck et al. 2020). Interestingly, the ring-like concentration cannot easily be explained with kinematic theory (Ruzmaikin et al. 1988), unless one invokes a similar variation of the gas density and thereby of $B_{\rm eq}$ (Beck et al. 1996). Such details have been ignored in our present modeling.

A potential shortcoming of the present calculations is that our predictions are based solely on mean-field dynamos. This means that we only take the large-scale component of the magnetic field into account. In reality, there is also a small-scale component whose helicity is expected to have the opposite sign (Blackman & Brandenburg 2003). How this affects the detection prospects of systematic E and B po-

larizations is currently unknown and should be a target of future investigations. The typical scale of fluctuations would not exceed 100 pc (Beck et al. 1996), which is well below the resolution scale of the James Clerk Maxwell Telescope. It is therefore possible that our present results may already give a good hint at what can be observed in the near future. Higher resolution observations would be of great interest for testing the idea of a magnetic helicity reversal at smaller length scales. In the meantime, however, it would be worthwhile to explore this regime of smaller length scales with detailed turbulence simulations without adopting mean field theory.

Another opportunity for improvements is given by our increased knowledge of the rotation curves of NGC 891 (Fraternali et al. 2011). In particular, it is now known that the rotation in the halo of NGC 891 is slower than that in the galactic disc (Oosterloo et al. 2007). This implies the presence of vertical shear that could modify the vertical helicity profile of the galaxy.

ACKNOWLEDGEMENTS

This work was supported in part through the Swedish Research Council, grant 2019-04234, and the National Science Foundation under the grant AAG-1615100. This research is partially supported by Grants-in-Aid for Scientific Researches from the Japan Society for Promotion of Science (KAKENHI 19H0193810). We acknowledge the allocation of computing resources provided by the Swedish National Allocations Committee at the Center for Parallel Computers at the Royal Institute of Technology in Stockholm.

APPENDIX A: E AND B FROM A PATCH IN Q

The purpose of this appendix is to compute the E and B polarization patterns for a signal with Stokes $U=0$ and Stokes Q originating from just a Gaussian patch of a projected horizontal or a vertical magnetic field. To also illuminate the question about different sign conventions, we use this opportunity to compare the local approach given by Eqs. (1) and (2) with the global one, where the complex polarization is expanded in terms of spin-2 spherical harmonic functions (e.g., Durrer 2008). We therefore work with spherical coordinates (θ,ϕ), where θ is colatitude and ϕ is longitude with $0<\theta<\pi$ and $0<\phi<2\pi$. We write the projected magnetic field in the form

$$B_{\phi/\theta}=B_0\exp\left\{-\left[(\theta-\theta_0)^2+(\phi-\phi_0)^2\right]/2\sigma^2\right\}, \tag{A1}$$

where we choose $\theta_0=\phi_0=\pi/2$ to be a point on the equator and $\sigma=10^\circ$ is chosen for the size of the patch. (The underlying three-dimensional magnetic field would be always solenoidal.) The global representations of E and B (indicated by subscripts 'glob') are expressed through the complex function

$$E_{\rm glob}+{\rm i}B_{\rm glob}\equiv R=\sum_{\ell=2}^{N_\ell}\sum_{m=-\ell}^{\ell}\tilde{R}_{\ell m}Y_{\ell m}(\theta,\phi), \tag{A2}$$

where the coefficients $\tilde{R}_{\ell m}$ are given by

$$\tilde{R}_{\ell m}=\int_{4\pi}(Q+{\rm i}U)\,{}_2Y^*_{\ell m}(\theta,\phi)\,\sin\theta\,{\rm d}\theta\,{\rm d}\phi. \tag{A3}$$

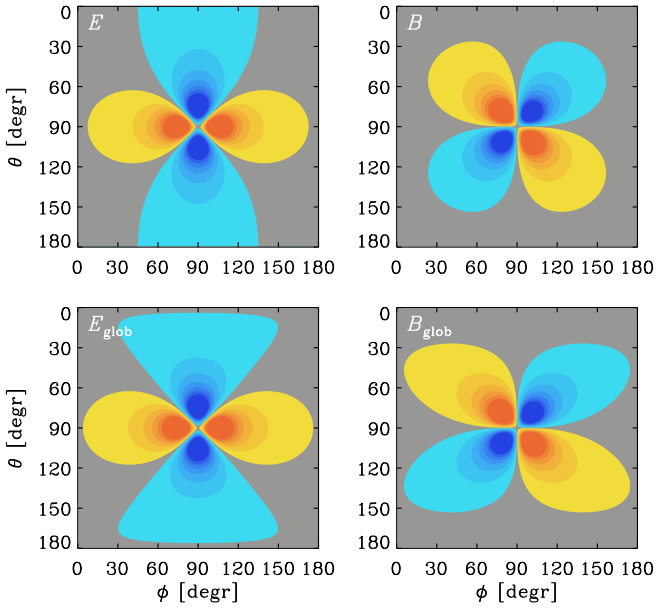

Figure A1. Local representations E and B together with their global counterparts $E_{\rm glob}$ and $B_{\rm glob}$ for a Gaussian patch with just a horizontal magnetic field, $\boldsymbol{B}=(0,B_\phi)$.

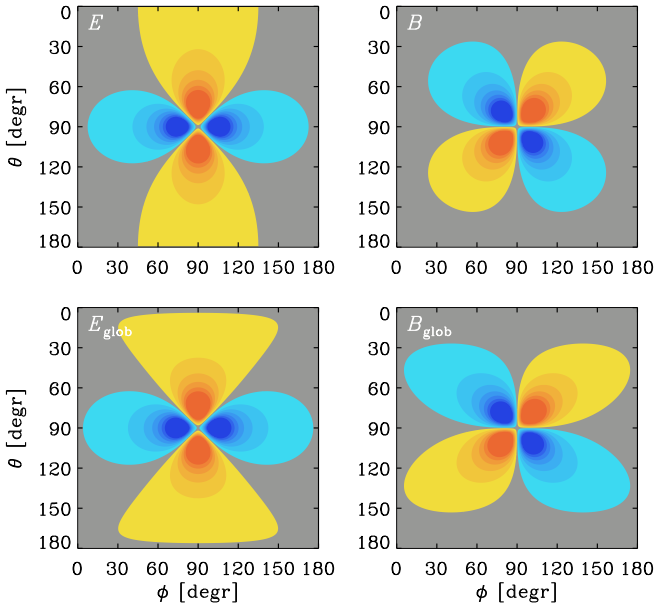

Figure A2. Same as Fig. A1, but for a vertical magnetic field, $\boldsymbol{B}=(B_\theta,0)$.

Here ${}_2Y^*_{\ell m}(\theta,\phi)$ are the spin-2 spherical harmonics of spherical harmonic degree ℓ and order m and the asterisk denotes complex conjugation. In the cosmological context, both $E_{\rm glob}$ and $B_{\rm glob}$ are defined with a minus sign; see, e.g., Eq. (6) of Zaldarriaga & Seljak (1997). The results for a Gaussian B_ϕ and a B_θ patch given by Eq. (A1) are shown in Figs. A1 and A2, using $N_\ell=36$ as the truncation level. We compare $E_{\rm glob}$ and $B_{\rm glob}$ with E and B in the range $0<\phi<\pi$, but the calculations have been done in the full range $0<\phi<2\pi$.

Both E and $E_{\rm glob}$ as well as B and $B_{\rm glob}$ agree with each other and are qualitatively similar to the overall appearance of E and B seen in Fig. 3. The agreement between local and global representations shows that for a single patch, the sign convention used in Durrer (2008) and Brandenburg (2019) for the global representation agrees with the local one used in BBKMRPS and Prabhu et al. (2020).

Interestingly, the cloverleaf-shaped pattern of B in Fig. A1 resembles a similar pattern found by BB20 for the Galactic center. A difference, however, is the sign of both E and B. In Fig. A2 we show that such a pattern can explained be by a case with a strong vertical magnetic field. As expected, the signs of both E and B are now changed and the resulting pattern matches that found BB20.

REFERENCES

Alton, P. B., Bianchi, S., Rand, R. J., Xilouris, E. M., Davies, J. I., & Trewhella, M. 1998, ApJ, 507, L125

Alton, P. B., Xilouris, E. M., Misiriotis, A., Dasyra, K. M., & Dumke, M. 2004, A&A, 425, 109

Andersson, B.-G., Lazarian, A., & Vaillancourt, J. E. 2015, ARA&A, 53, 501

Beck, R., Chamandy, L., Elson, E., & Blackman, E. G. 2019, Galaxies, 8, 4

Beck, R., Brandenburg, A., Moss, D., Shukurov, A., & Sokoloff, D. 1996, ARA&A, 34, 155

Beck, R., Berkhuijsen, E. M., Gießübel, R., & Mulcahy, D. D. 2020, A&A, 633, A5

Blackman, E. G., & Brandenburg, A. 2003, ApJ, 584, L99

Bocchio, M., Bianchi, S., Hunt, L. K., & Schneider, R. 2016, A&A, 586, A8

Bracco, A., Candelaresi, S., Del Sordo, F., & Brandenburg, A. 2019a, A&A, 621, A97

Bracco, A., Ghosh, T., Boulanger, F., & Aumont, J. 2019b, A&A, 632, A17

Brandenburg, A. 2015, in Magnetic fields in diffuse media, ed. E. de Gouveia Dal Pino & A. Lazarian (Astrophys. Spa. Sci. Lib., Vol. **407**, Springer), 529

Brandenburg, A. 2019, ApJ, 883, 119

Brandenburg, A. 2019, in IAUS 354: Solar and Stellar Magnetic Fields: Origins and Manifestations, ed. A. Kosovichev, K. Strassmeier & M. Jardine (Proc. IAU Symp., Vol. **354**), in press

Brandenburg, A., & Brüggen, M. 2020, ApJL, submitted, arXiv:2003.14178 (BB20)

Brandenburg, A., & Dobler, W., Pencil Code, `http://ui.adsabs.harvard.edu/abs/2010ascl.soft10060B` DOI:10.5281/zenodo.2315093.

Brandenburg, A., & Stepanov, R. 2014, ApJ, 786, 91

Brandenburg, A., Bracco, A., Kahniashvili, T., Mandal, S., Roper Pol, A., Petrie, G. J. D., & Singh, N. K. 2019, ApJ, 870, 87 (BBKMRPS)

Brandenburg, A., Donner, K. J., Moss, D., Shukurov, A., Sokoloff, D. D., & Tuominen, I. 1992, A&A, 259, 453

Brandenburg, A., Donner, K. J., Moss, D., Shukurov, A., Sokoloff, D. D., & Tuominen, I. 1993, A&A, 271, 36

Brandenburg, A., Krause, F., Meinel, R., Moss, D., & Tuominen, I. 1989, A&A, 213, 411

Chamandy, L., Shukurov, A., & Subramanian, K. 2015, MNRAS, 446, L6

Crutcher, R. M. 2012, ARA&A, 50, 29

Durrer, R. 2008, The Cosmic Microwave Background (Cambridge: Cambridge University Press)

Elstner, D., Golla, G., Rüdiger, G., & Wielebinski, R. 1995, A&AS, 297, 77

Fraternali, F., Sancisi, R., & Kamphuis, P. 2011, A&A, 531, A64

Haas, M., Klaas, U., & Bianchi, S. 2002, A&A, 385, L23

Han, J. L. 2017, ARA&A, 55, 111

Hildebrand, R. H., Kirby, L., Dotson, J. L., Houde, M., & Vaillancourt, J. E. 2009, ApJ, 696, 567

Horellou, C., & Fletcher, A. 2014, MNRAS, 441, 2049

Howk, J. C., & Savage, B. D. 1999, AJ, 117, 2077

Hughes, T. M., Baes, M., Fritz, J., Smith, M. W. L., Parkin, T. J., et al. 2014, A&A, 565, A4

Ivanova, T. S., & Ruzmaikin, A. A. 1977, Sov. Astron., 21, 479

Jones, T. J., Dowell, C. D., Lopez Rodriguez, E., Zweibel, E. G., Berthoud, M., et al. 2019, ApJ, 870, L9

Junklewitz, H., & Enßlin, T. A. 2011, A&A, 530, A88

Kahniashvili, T., Maravin, Y., Lavrelashvili, G., & Kosowsky, A. 2014, PhRvD, 90, 083004

Kamionkowski, M., & Kovetz, E. D. 2016, ARA&A, 54, 227

Kamionkowski, M., Kosowsky, A., & Stebbins, A. 1997, PhRvL, 78, 2058

Krause, F., & Rädler, K.-H. 1980, Mean-field Magnetohydrodynamics and Dynamo Theory (Oxford: Pergamon Press)

Krause, M. 2019, Galaxies, 7, 54

Krause, M., Irwin, J., Schmidt, P., Stein, Y., Miskolczi, A., Mora-Partiarroyo, S. C., Wiegert, T., Beck, R., Stil, J. M., Heald, G., Li, J.-T., Damas-Segovia, A., Vargas, C. J., Rand, R. J., West, J., Walterbos, R. A. M., Dettmar, R.-J., English, J., Woodfinden, A. 2020, A&A, in press, arXiv:2004.14383

Matthews, B. C., McPhee, C. A., Fissel, L. M., & Curran, R. L. 2009, ApJS, 182, 143

Moffatt, H. K. 1978, Magnetic Field Generation in Electrically Conducting Fluids (Cambridge: Cambridge Univ. Press)

Moss, D., & Sokoloff, D. 2017, A&A, 598, A72 Galactic winds and the origin of large-scale magnetic fields

Oosterloo, T., Fraternali, F., & Sancisi, R. 2007, ApJ, 134, 1019

Oppermann, N., Junklewitz, H., Robbers, G., & Enßlin, T. A. 2011, A&A, 530, A89

Parker, E. N. 1955, ApJ, 122, 293

Parker, E. N. 1971, ApJ, 163, 255

Pattle, K., & Fissel, L. 2019, Front. Astron. Space Sci., 6, 1

Planck Collaboration Int. XIX. 2015, A&A, 576, A104

Prabhu, A., Brandenburg, A., Käpylä, M. J., & Lagg, A. 2020, A&A, submitted, arXiv:2001.10884

Rüdiger, G. 1978, Astron. Nachr., 299, 217

Ruzmaikin, A. A., Sokoloff, D. D. & Shukurov, A. M. 1988, Magnetic Fields of Galaxies (Kluwer, Dordrecht)

Seljak, U., & Zaldarriaga, M. 1997, PhRvL, 78, 2054

Shukurov, A. 1998, MNRAS, 299, L21

Sokoloff, D. D., & Shukurov, A. M. 1990, Nature, 347, 51

Steenbeck, M., Krause, F., & Rädler, K.-H. 1966, Z. Naturforsch., 21a, 369

Strickland, D. K., Heckman, T. M., Colbert, E. J. M., Hoopes, C. G., & Weaver, K. A. 2004, ApJ, 606, 829
Vainshtein, S. I., & Ruzmaikin, A. A. 1971, Sov. Astron., 16, 365
Volegova, A. A., & Stepanov, R. A. 2010, Sov. Phys. JETP, 90, 637
Ward-Thompson, D., Pattle, K., Bastien, P., Furuya, R. S., Kwon, W., Lai, S.-P., Qiu, K., Berry, D., Choi, M., Coudé, S., Di Francesco, J., Hoang, T., Franzmann, E., Friberg, P., Graves, S. F., Greaves, J. S., Houde, M., Johnstone, D., Kirk, J. M., Koch, P. M., et al. 2017, ApJ, 842, 66
Whaley, C. H., Irwin, J. A., Madden, S. C., Galliano, F., & Bendo, G. J. 2009, MNRAS, 395, 97
Wiegert, T., Irwin, J., Miskolczi, A., Schmidt, P., Mora, S. C., Damas-Segovia, A., Stein, Y., English, J., Rand, R. J., Santistevan, I., Walterbos, R., Krause, M., Beck, R., Dettmar, R.-J., Kepley, A., Wezgowiec, M., Wang, Q. D., Heald, G., Li, J., MacGregor, S. , et al. 2015, AJ, 150, 81
Zaldarriaga, M. & Seljak, U. 1997, PhRvD, 55, 1830